

Coupling direct powder deposition with spark plasma sintering: a new approach towards rapid prototyping

Original

Coupling direct powder deposition with spark plasma sintering: a new approach towards rapid prototyping / Airoidi, L.; Brucculeri, R.; Baldini, P.; Morganti, S.; Actis Grande, M.; Gobber, F. S.; Auricchio, F.; Anselmi-Tamburini, U.. - In: PROGRESS IN ADDITIVE MANUFACTURING. - ISSN 2363-9512. - ELETTRONICO. - (2024). [10.1007/s40964-023-00552-2]

Availability:

This version is available at: 11583/2987983 since: 2024-04-22T11:40:07Z

Publisher:

Springer

Published

DOI:10.1007/s40964-023-00552-2

Terms of use:

This article is made available under terms and conditions as specified in the corresponding bibliographic description in the repository

Publisher copyright

(Article begins on next page)



Coupling direct powder deposition with spark plasma sintering: a new approach towards rapid prototyping

L. Airoidi² · R. Brucculeri² · P. Baldini¹ · S. Morganti³ · M. Actis Grande⁴ · F. S. Gobber⁴ · F. Auricchio² · U. Anselmi-Tamburini¹

Received: 28 March 2023 / Accepted: 17 November 2023
© The Author(s) 2024

Abstract

In this paper, we propose a modified material jetting technology based on a piezoelectric-driven powder deposition, hence direct powder deposition (DPD), combined with pressure-assisted rapid sintering. This is a new approach toward the rapid production of metal and ceramic materials with complex geometries. The combined deposition of two loose powders within the same container, layer by layer, allows realizing complex shapes without the use of any binder or dispersing medium. The resulting green sample is then sintered by field assisted sintering (FAST) or spark plasma sintering (SPS) operating in a pseudo-isostatic mode. This combination of DPD and FAST/SPS allows great versatility, as it can be extended to a wide range of materials and composites without any significant modification of the setup. Moreover, the use of FAST/SPS densification allows the realization of fully sintered samples in less than one hour.

Keywords Additive manufacturing · Direct powder deposition · Spark plasma sintering · Powder rheology

1 Introduction

Additive manufacturing is receiving wide attention as an alternative to traditional powder technology for the rapid production of metal components with reduced costs and environmental impact.

Over the past two decades, powder bed fusion (PBF) has become the de facto industry standard for additive metal production. However, PBF technologies still suffer from considerable limitations. Despite their widespread use, printers

are still expensive and difficult to operate. Moreover, they present limited versatility, as the transition from one material to another is generally complex and time-consuming [1–7]. Furthermore, the rapid heating and cooling cycles typical of these techniques can introduce significant differences between the characteristics of materials produced through this route and the same materials obtained using conventional manufacturing techniques [8–10]. Some attempts have been made to address these problems [11, 12], but the impact of these solutions is still limited. Alternative additive

✉ L. Airoidi
lorenzo.airoidi01@universitadipavia.it

R. Brucculeri
riccardo.brucculeri01@universitadipavia.it

P. Baldini
primo.baldini@unipv.it

S. Morganti
simone.morganti@unipv.it

M. Actis Grande
marco.actis@polito.it

F. S. Gobber
federico.gobber@polito.it

F. Auricchio
auricchi@unipv.it

U. Anselmi-Tamburini
tau@unipv.it

¹ Department of Chemistry, University of Pavia, V.le Taramelli 12, 27100 Pavia, Italy

² Department of Civil Engineering and Architecture, University of Pavia, Via Ferrata 3, 27100 Pavia, Italy

³ Department of Electrical, Computer, and Biomedical Engineering, University of Pavia, Via Ferrata 5, 27100 Pavia, Italy

⁴ Department of Applied Science and Technology (DISAT), Polytechnic of Turin, Viale T. Michel 5, 15121 Alessandria, Italy

manufacturing approaches have been proposed in the last two decades, all requiring a medium to disperse the solid powder to be printed. Examples are the polymeric binders used in the material extrusion (MEX) [13] or the photopolymerizing or thermal binders used in binder jetting (BJT), material jetting (MJT) and vat photopolymerization (VPP) technologies [14, 15]. All these methods require a binder removal (debinding) at the end of the printing process, followed by a sintering step. Typically performed in an oven, these processes might take a considerable time and sometimes require a preliminary chemical attack involving the use of organic solvents or other chemical moieties.

Here, we present an innovative and versatile material jetting technology that is based on the deposition of loose powders using a piezoelectric-driven dispenser. Hence, the name direct powder deposition (DPD).

The combined deposition of two powders, layer by layer, allows realizing the shape of the final object without the addition of any dispersing medium. This technology can be combined with both classical densification procedures (such as cold pressing and/or conventional sintering) or with more advanced sintering techniques. In this work, the direct powder deposition is combined with pressure-assisted field assisted sintering (FAST) or spark plasma sintering (SPS) [16, 17], performed in a pseudo-isostatic mode. The absence of elements outside the powder of interest guarantees the compositional purity of the final objects. In addition, FAST/SPS sintering opens the possibility of achieving very high final density values and obtaining finished objects in just a few minutes.

2 Materials and methods

2.1 Powders characterization

Two types of powders have been used in this work. One for the realization of the required object and one for containment and pressure transfer. The first material was an AISI 316L powder (15 to 45 μm grain size) supplied by Mimete s.r.l. (MARS 316L cat. n. 1220078G014). The second powder was coarse Al_2O_3 with a grain size ranging between 50 and 150 μm , supplied by Sigma-Aldrich (cat. n. 06300). Before printing, this last powder was sieved (FRITSCH 80 μm mesh No. 30.5640.03) to remove the fraction above 80 μm .

The powder morphology has been characterized by SEM using a microscope Tescan MIRA operated at 20 kV. The particle size distribution (PSD) was measured by laser diffraction methods (Malvern Mastersizer 3000), and the rheological properties were assessed either by traditional funnel standardized tests [18–20] or by shear cell methods with a rheometer (Freeman Technology FT4). The Hall funnel was employed to characterize flowability for both

materials. The same volume of loose powders (10 mm^3) was employed for steel and alumina. For the rheological characterization, the standard built-in testing programs were employed to characterize the flowability parameters of the bulk, the dynamic flow, and the shear properties (in accordance with ASTM D7981). Three repetitions were performed per each testing procedure.

Compressibility testing procedure: using a glass drum of 50 mm diameter and 85 mL volume, the powder was stirred initially for uniform distribution with a 48 mm blade. Controlled normal stresses were then applied via an exhaust piston featuring a stainless-steel woven mesh surface. This design ensures even release of entrapped air from the powder bed's surface. Each stress level, ranging from 0.5 to 15.0 kPa, was applied until equilibrium was achieved, measured by piston displacement. Compressibility was automatically quantified as a percentage of volume change using the vessel's known volume. This approach facilitates the calculation of powder compressibility density under varying normal phase pressures.

Shear test method: employing a glass cylinder of 50 mm diameter and 85 mL volume, the measurement process involves a rotary unit module containing powder samples and a shearing head. The shearing head generates both vertical and rotary stress by descending into the powder. As it contacts the powder surface, normal stress is created. Upon reaching the target normal stress of 3, 6, or 9 kPa, the shearing head initiates slow rotation, inducing shear stress just beneath the blade ends.

Wall friction: this assessment incorporates a container holding powder samples and a specialized wall friction head, designed to induce vertical and rotational stresses. Utilizing a glass cylinder with a 50 mm diameter and an 85 mL volume as the vessel, the wall friction head descends onto the powder surface, initiating normal stress upon breaking contact with the top powder layer. Its downward movement continues until the prescribed normal stress level is attained. Within our experiments, we maintain normal stresses of 3, 6, and 9 kPa.

Subsequently, while keeping the normal stress constant, controlled rotation of the wall friction head begins, generating shear stress and forming a distinct shear plane between the disk and the powder surface. The torque needed to counter the resistance of the powder bed against the wall friction head's rotation progressively rises until it overcomes the resistance entirely, marking the point of maximum torque. The friction head maintains a steady rotational speed for a predefined period. The measurement of the torque required to sustain this rotation enables the calculation of "steady-state" shear stress. This shear stress is linked to the normal stress to deduce the wall friction angle between the powder and the wall friction head.

Stability and flow rate testing: the standard stability assessment combines adjustment and test cycles to gauge potential powder alterations due to flow dynamics. This evaluation was conducted within a 50 mm diameter glass cylinder with a 160 mL volume. Initial stirring with a 48 mm blade tracked energy fluctuations during the process. Seven test cycles, all executed at a 100 mm/s tip speed, compose the stability test. The powder's stability is evident in energy changes across these cycles—stable powder retains consistent energy shifts, while unstable powder demonstrates pronounced variations.

The stabilized energy from the seventh test cycle serves as the baseline flowability energy (BFE), defining the energy required to induce a specific flow pattern through the conditioned powder bed in downstream testing. This pattern involves a downward anti-clockwise blade motion, generating a relatively high-stress compressive flow mode within the powder. The ratio of the sixth and seventh cycle's average energy to the sample mass quantifies the specific energy (SE), a measure of powder flow in unconstrained or low-stress environments. SE characterizes the unconstrained or low-stress flow state, predominantly reflecting interparticle bonding forces.

The PSD of the steel powders were characterized as received, due to their acceptable flowability, while alumina powders were characterized both as received and after sieving to remove the fraction of powders larger than 80 μm .

2.2 Printing setup

The deposition of the two powders was realized using a modified CNC platform (Openbuild QueenBee PRO kit). In this configuration, a graphite die was connected, with its lower plunger inserted, to a head that moves in the XY plane (Fig. 1a). This movement controls the spatial distribution of the two powders on each layer. The Z movement, required to move from one layer to the following, is obtained by lowering the plunger within the die. Two powder dispensers are fixed on the frame of the CNC, hovering just above the higher edge of the die. With this configuration, the deposition plane remains fixed in its Z position, aligned with the upper edge of the die and always at the same distance from the powder dispensers. Once a layer is completed, the plunger is lowered by an amount corresponding to the thickness of one layer and the deposition process is repeated.

Components movements were controlled by a Duet 2 Wi-Fi board which also controlled the 3D movements. The open-source software Ultimaker Cura Slicer has been used to generate *g.codes* from CAD models and to regulate the printing parameters.

The printing speed for the two types of powders (33.5 mm s^{-1} for AISI 316L and 20 mm s^{-1} for alumina) was adjusted to equalize the volume of powders dispensed in the unit

time. The layer height was set to 0.28 mm and the line width to 0.4 mm for both materials.

The powder dispensers (Fig. 1c, d) were realized using two syringes (Nordson EFD) with a conical needle presenting an aperture of 0.400 mm (Nordson Optimum[®] SmoothFlow[™] 7,018,298). The vibration of the piezoelectric actuators (PICMA[®] piezo actuator P-882.11) is transferred to a nut in which the needle tip rests in. Vibrations cause an elastic deformation of the tip on the needle and force the powders to flow through the aperture.

In the rest position, when piezoelectric actuators are off, there is no powder flow. Additional photos of the printer and a video of the machine operating can be found in Online Resources 1–2. The vibrations of the piezoelectric actuators have been controlled using a wave generator (Analog Discovery 2 by Digilent) connected to an in-house built amplifier to boost the amplitude of the generated signal.

2.3 Heat treatments (FAST/SPS sintering)

The sintering process was performed using a custom-made FAST/SPS machine. A schematic of the setup is reported in Fig. 2. The graphite die containing the deposited powders was placed between two hydraulic rams also acting as electrodes. Sintering routine to obtain maximum density is based on our previous work [21]. A pressure of 25 MPa was applied at this stage. The sintering cycle was conducted under a dynamic vacuum of 10 Pa. A linear heating ramp from room temperature to 1150 °C, with a rate of 100 °C min^{-1} , was realized through an electric current flowing directly through the die. When the temperature reached 1150 °C the applied pressure was increased to 50 MPa. After 5 min the pressure was released, and the setup allowed to cool freely. In total, the sintering cycle lasts for less than 1 h. At the end of the process, the sample was removed from the graphite die. The thermal cycle allowed only for the sintering of the AISI 316L powder. The coarse alumina powder resulted unaffected, acting only as a pressure transfer medium and could be easily removed. To completely remove the alumina powder residue, the metallic sintered object was then sandblasted.

3 Result and discussion

3.1 Powders characterization

The morphology of the two powders used in this study is shown in the SEM images of Fig. 3. The AISI 316L powder is obtained by gas atomization and presents mostly spherical grains. The Al_2O_3 powder, on the other end, presents grains with a more irregular shape that appear to be agglomerates of smaller faceted crystals.

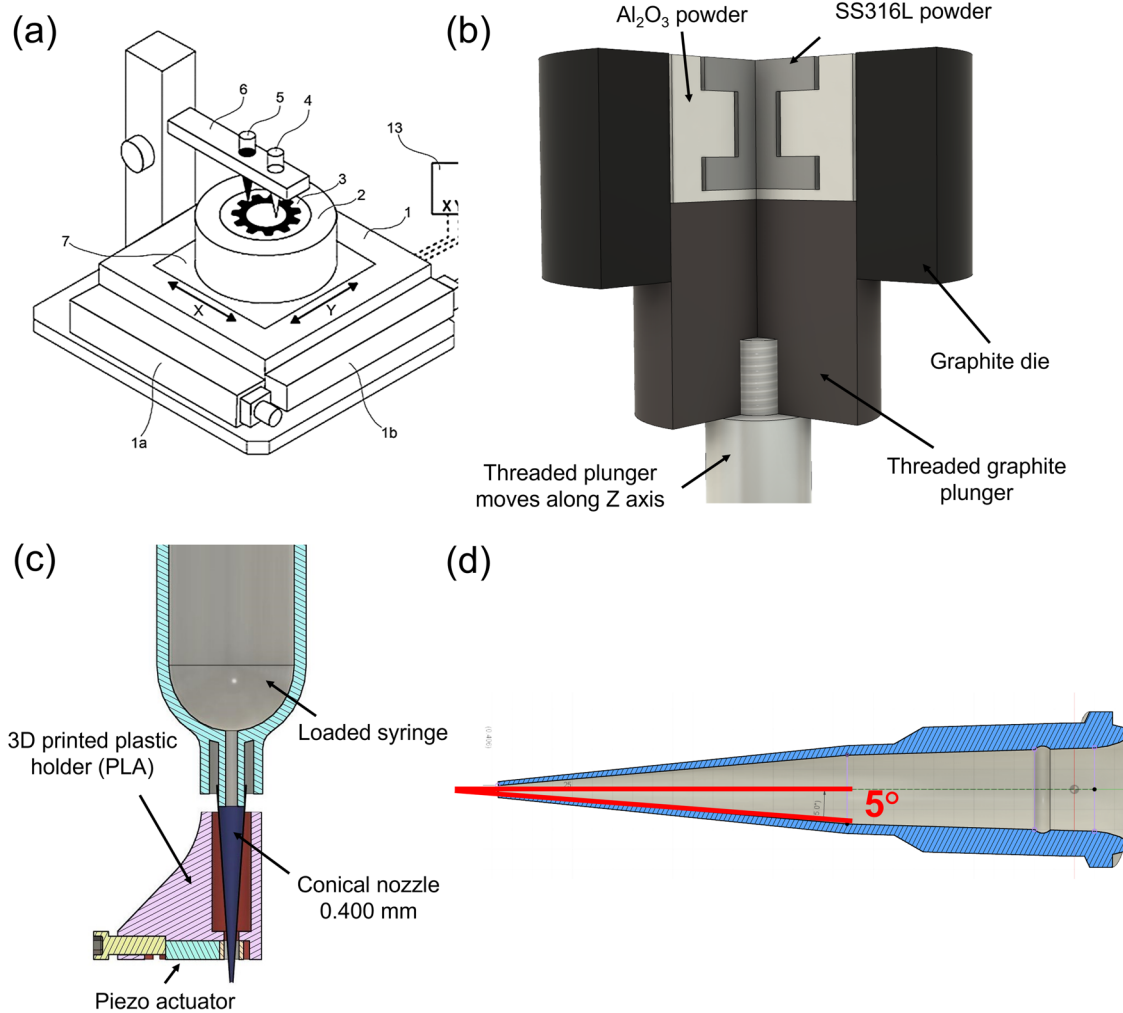


Fig. 1 **a** Diagram of the printhead, the moving carriage moves the graphite plunger inside the fixed graphite die. **b** Cross-section of the situation of the two powders deposited in the graphite assembly (die

with plunger) during printing operation. **c** Close-up of the piezo-actuated syringe with all main components labeled and **d** geometry of the conical nozzle

Powder rheology plays a key role in determining powder flowability, a complex parameter that depends on the properties of the powder itself (particle size distribution, morphology, density, and surface interaction) and on several external factors (humidity, temperature, and atmosphere) [22]. To obtain good control of the deposition process, powders must exhibit interparticle forces slightly greater than the gravitational force to create a stable dome at the needle tip when the system is at rest but being small enough to not clog the nozzle. In this respect, the needle aperture is a key parameter. Our preliminary observations have shown that to form a stable dome, the powders must present a grain size 5 to 8 times smaller than the needle aperture. In this way, powder grain can still smoothly flow when vibrated. For this reason, the alumina powder (Fig. 3c, d) was sieved to largely reduce particles larger than 80 μm in diameter. When the piezo-vibrator

is activated, the stable but fragile inter-particle structure breaks down, forcing the powder to fall.

The grain size distribution of the two powders is reported in Fig. 4. The amount of large particles present in the alumina powder decreases after sieving, as shown by the PSD and by the granulometric indicators reported in Table 1. However, a significant amount of powders larger than 80 μm is still present even in the sieved alumina sample. The span value represents the PSD shape. The larger the span, the higher the asymmetry of the PSD curve. Despite sieving, the span of the alumina decreases only from 1.4 to 1.2 due to the high-volume fraction of very fine particles (Fig. 4). As metal powders are regarded, a span lower than 1.5 is generally considered as an indicator of good flowability [23]. Such indication is confirmed for the powders analyzed, with 316L powders having a low span and the highest Hall flowability. Considering the D_{100} descriptor (see Table 1)

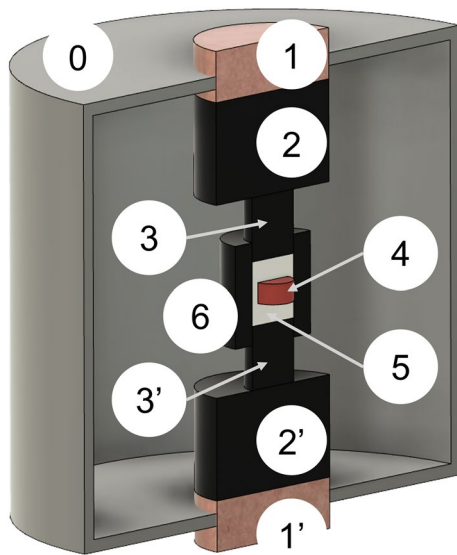


Fig. 2 SPS vacuum chamber (0) set to work in pseudo-isostatic mode. A hydraulic system produces the uniaxial pressure required during the densification. The two hydraulic pistons (1–1') act as electrodes to supply current first to graphite pistons (2–2') and so to graphite plungers (3–3'). The current flux is generated by a high-power transformer that produces a maximum current of 5000 A at 6 V. The two powders (4, 5) are confined into the graphite die (6). The temperature is controlled by a K-type thermocouple inserted in the lateral wall of the graphite die

for the unsolved alumina powders, a value close to half the nozzle aperture diameter (400 μm) was detected. Such large particles can clog the dosing syringe resulting in an intermittent deposition or, at worse, stopping the powder flow completely.

From the standard flowability descriptors (Table 2), a difference between steel and alumina arises, indicating a slightly higher flowability of steel. Apart from the metallic nature of the powders themselves, the spherical shape reduces the occurrence of interlockings while more angular and faceted particles, such as the one presented by alumina, are more prone to interlocking when flowing.

Despite these small differences, the two powders are comparable in terms of flowability if standard descriptors are considered. Furthermore, comparable results were observed for alumina powders tested with the same rheometer when considering comparable particle size distributions [24, 25].

Based on the Hausner Ratio (HR), all three powders' behavior falls in group A, describing free-flowing or easily fluidizable powders [26, 27].

Another important parameter is represented by the density achieved by the powders when deposited with our setup. Surprisingly, the density of the deposited powders is close to the tap density and is significantly higher than the apparent density of loose powders. Probably our process allows the deposition of a thin layer of randomly

distributed and well-packed particles. This result improves the final relative density attainable using this method [28, 29].

Some systematic differences between the two powders arise from the rheological characterization carried out with the shear cell rheometer (Fig. 5). The higher flow energies, expressed in mJ, for steel (Fig. 5a) are related to its higher bulk density as more energy is required for the rheometer blade to travel inside the powder sample.

The two powders show a different trend under variable flow rate testing, with alumina being less sensitive to a decrease in tip speed. The most interesting finding concerns the alumina powder compressibility (CPS%) reported in Fig. 5b. The numerous gaps in the unsieved powders allow higher packing, reducing its flowability. The CPS% value is comparable between the three powders; however, the different nature of the powders (ceramic vs metallic), the different morphology (irregular vs spherical), and the different PSD must be considered. These factors increase the metallic powder flowability despite comparable compressibility values. In addition, the metallic powder can be deformed and thus increase its compressibility.

As the applied pressure increases, ceramic powder is rather insensitive to normal stress, while metallic powder tends to compress more as the applied stress increases.

SEM imaging reveals that the only constant factor before and after sieving the alumina powders is the surface roughness and topology, which play a key role in the formation of bridges and interlocking. This observation is further supported by studies in the literature, which have demonstrated that irregular morphology leads to more surface contacts, generating frictional forces that impede flow [30, 31]. This behavior is confirmed by a rheological indicator, the angle of internal friction (AIF) depicted in Fig. 5d, which is higher for alumina powders. This indicator is directly associated with the movement of powders as they flow through the Hall funnel or the direct powder deposition nozzle.

During the direct powder deposition process, the metallic and ceramic powders are dispensed through a conical nozzle that must prevent powders from flowing freely, if not intended. The conical nozzle is a tiny axisymmetric polyethylene hopper with a geometry similar to the one reported in Fig. 1d. By employing the method described in [32], the hopper half angle (α) preventing powders from free-flowing was calculated from experimental data for each powder using Eq. (1)

$$\alpha = \frac{\pi}{2} - \frac{1}{2} \left(\frac{1 - \sin \delta}{2 \sin \delta} \right) - \beta \quad (1)$$

where δ is the effective angle of internal friction (AIF), calculated experimentally by shear cell testing, and β is a parameter calculated after Eq. (2)

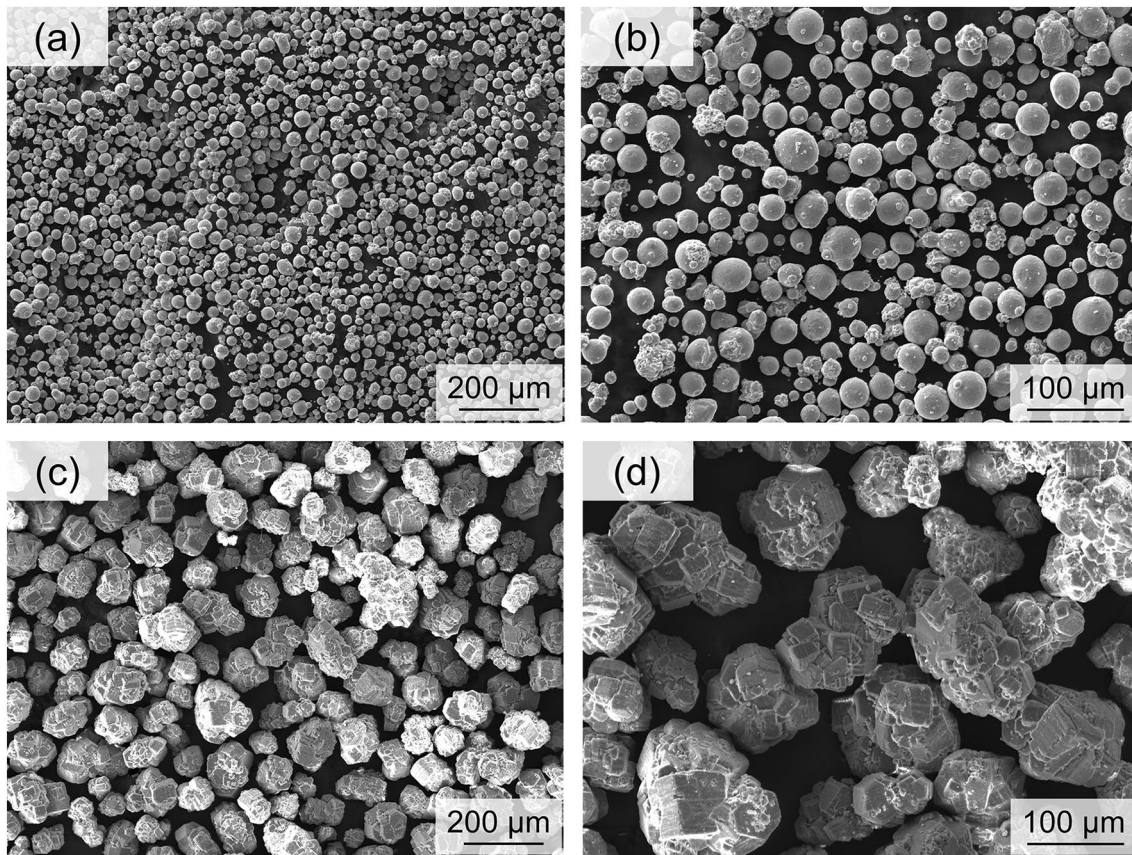


Fig. 3 SEM images of the AISI 316L (a, b) and the pristine Al_2O_3 powders (c, d) used in this work

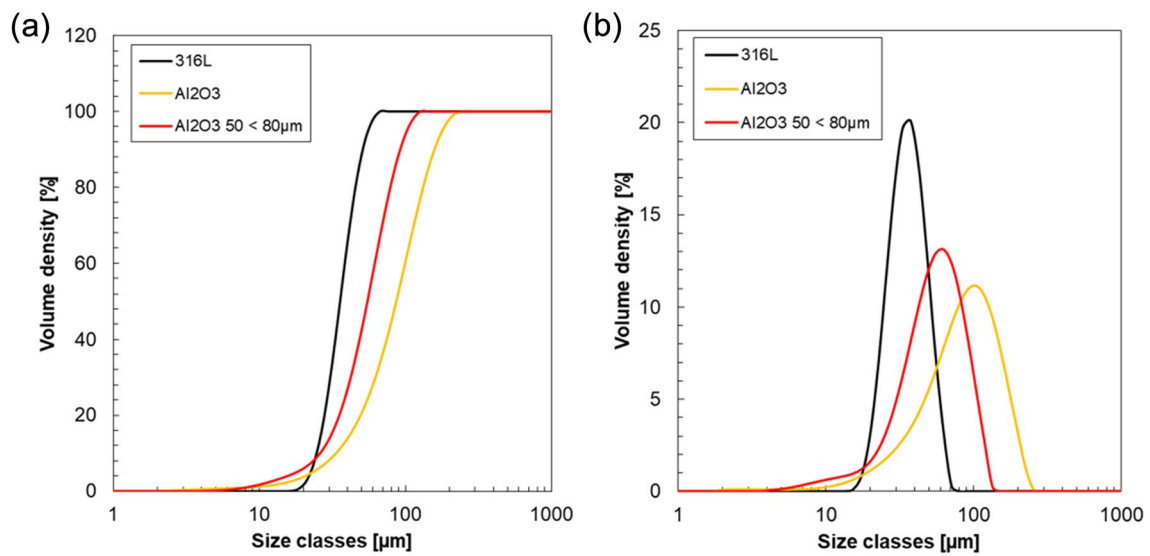


Fig. 4 Powder granulometry as **a** cumulative PSD and **b** general PSD

Table 1 Particle size descriptors for the extended PSD curve

	D ₁₀ [μm]	D ₅₀ [μm]	D ₉₀ [μm]	Mode [μm]	Span	D ₁₀₀ [μm]
316L	24.7	35.8	51.2	35.0	0.7	73.7
Al ₂ O ₃	35.9	89.6	162.6	103.9	1.4	253.6
Al ₂ O ₃ sieved	25.9	55.0	93.2	60.9	1.2	140.7

Table 2 Densities and flowability descriptors for the steel and alumina powder tested under different conditions

Density (g cm ⁻³)	AISI 316L	Alumina <80 μm	Alumina Al ₂ O ₃
Bulk material	7.99	3.95	3.95
Apparent density	4.01	0.92	0.95
Tap density	4.80	1.11	1.01
Deposited powders	4.89	1.08	–
Hausner ratio (HR)	1.19	1.20	1.06
Hall flowability [s]	14.01	18.73	18.54

$$\beta = \frac{1}{2} \left\{ \varphi + \frac{\sin \sin \varphi}{\sin \sin \delta} \right\} \quad (2)$$

where φ is the wall friction angle, calculated experimentally using the wall friction module of the rheometer with polyethylene disks ($R_a = 0.01 \mu\text{m}$) simulating the nozzle walls. This value relates the shear stress at the hopper wall to the corresponding normal stress applied.

All the tested powders do not freely flow when packed inside the nozzle. From the shear properties of the powders, the angle (α) and the orifice diameter (D) to have a mass-flow regime have been calculated and reported in Table 3. Interestingly, alumina powders show a lower major consolidating stress (σ_1) than steel but higher unconfined compressive strength (σ_{1C}) and wall friction (φ) against polyethylene. With the adopted design that is constituted by a nozzle with an angle of 5° and an aperture of 0.400 mm the powders do not freely flow. This is in accordance with the shear cell measurements. Such a small orifice is needed to confine the powder flow to maximize the deposition accuracy. The nozzle angle of 5° strongly favors powders to flow freely, being significantly lower than the minimum calculated value of $\approx 48^\circ$, but the second condition for mass flow is not respected in static conditions because the nozzle orifice is two orders in magnitude lower than the calculated one (0.400 mm vs 40 mm).

However, when the piezo-vibration is activated, all three powders flow despite different regimes. Specifically, continuous flow is observed for steel and sieved alumina, while discontinuous for unsieved alumina powder. Such behavior is supposed to be related to the interlockings between the particles clogging the nozzle.

Describing the rheological properties of vibrated powders is a non-trivial topic currently being investigated in the

literature [33, 34]. To the author's best knowledge, a robust and general model correlating vibration frequency, hopper geometry, and powder characteristics to the flow regime has not been developed yet and is out of this work's scope. Two different experimental methods to characterize the internal stresses in vibrated powders are presented in [35, 36], but systematic correlation with particle characteristics has not been presented. Vibrations induced on the nozzle can decrease both the yield strength of powders by up to 25% and the wall friction between powders and the hopper generating flows at much smaller outlet diameters than static conditions would permit [37].

3.2 Powder deposition process

We performed a characterization of the powder flow that can be obtained with the piezoelectric-driven device used in this work, to identify its optimal operational conditions. The parameters controlling the deposition process were: the vibrating frequency of the nozzle, its waveform (square or sinusoidal), and its amplitude, defined by the voltage applied to the piezoelectric actuator. We also characterized the time stability of the powder flow. Three to four repetitions were performed for each testing condition.

First of all, in accordance with the literature [38, 39], we observed that a more reliable powder micro-feeding was always obtained using a square waveform. The influence of its frequency has been investigated by analyzing the mass deposition rate during frequency sweeps performed between 2 and 35 kHz at a constant voltage of 7.8 V and for a fixed 10 s of extrusion time (Fig. 6a, b). The figure shows how the mass of deposited powder remains roughly constant within the explored range of frequencies, with the exception of some notable peaks. In particular, one sharp increase for the deposition of the AISI 316L centered at 22 kHz and two spikes for alumina centered at 12 and 25 kHz respectively, can be observed. We believe that these values correspond to the natural resonance frequency [11, 39] of the depositing nozzle for that specific material. This conclusion is supported by the analysis of slow-motion videos of the powder flowing through the nozzle recorded at 240 fps. These images show that choosing a frequency away from the main peaks (i.e., 5 kHz for AISI 316L and 20 kHz for Al₂O₃) (see Online Resource 3, 4), is possible to achieve a narrow and stable stream of powders flowing through the nozzle in response to the activation and deactivation path of

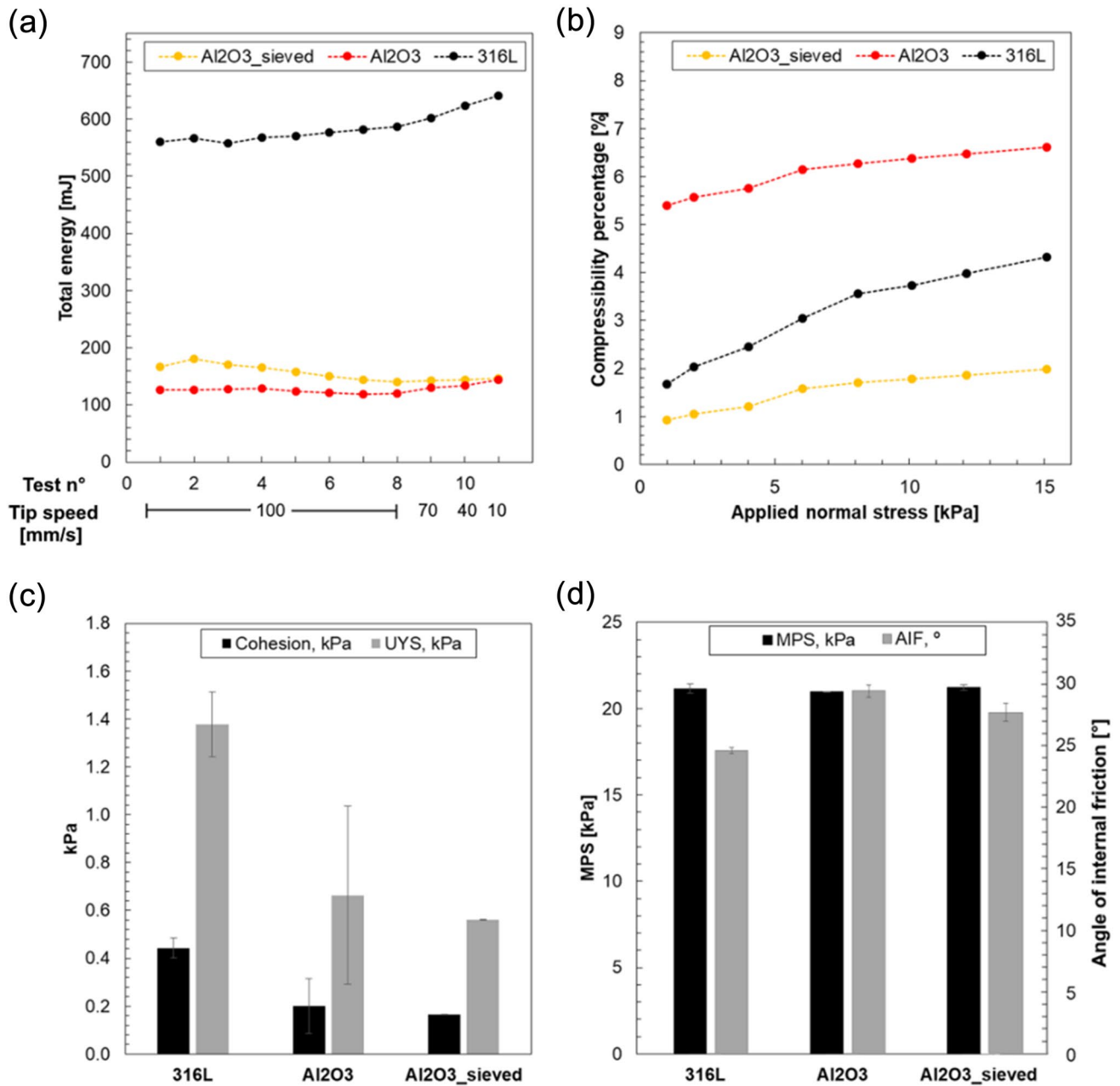


Fig. 5 Rheological indicators for the analyzed powders. **a** Split rate+variable flow rate, **b** compressibility 1–15 kPa, **c** cohesion, unconfined yield stress, and **d** major principal stress, angle of internal friction

Table 3 Geometric parameters for hopper characterization and notable rheological characteristics for the powders

	AISI 316L	Alumina <80 μm	Alumina Al ₂ O ₃
α	47.7	47.74	47.9
D [m]	0.03	0.04	0.08
σ_1 [kPa]	0.49	0.15	0.26
σ_{1C} [kPa]	5.02	18.2	12.65
ϕ	9.6	12.65	12.23
Flow factor (σ_1/σ_{1C})	2.46	2.73	3.29

the piezoelectric device. But excitation at frequencies corresponding to the peaks at 22 kHz for AISI 316L (Online Resource 5) and 25 kHz for Al₂O₃ (Online Resource 6) induces a “water-sprinkler” shape of the jetted powders, increasing the amount of deposited mass, but reducing the resolution of the deposition process.

Moreover, in six out of fifteen frequencies, we observed an unreliable deposition process. At these frequencies the

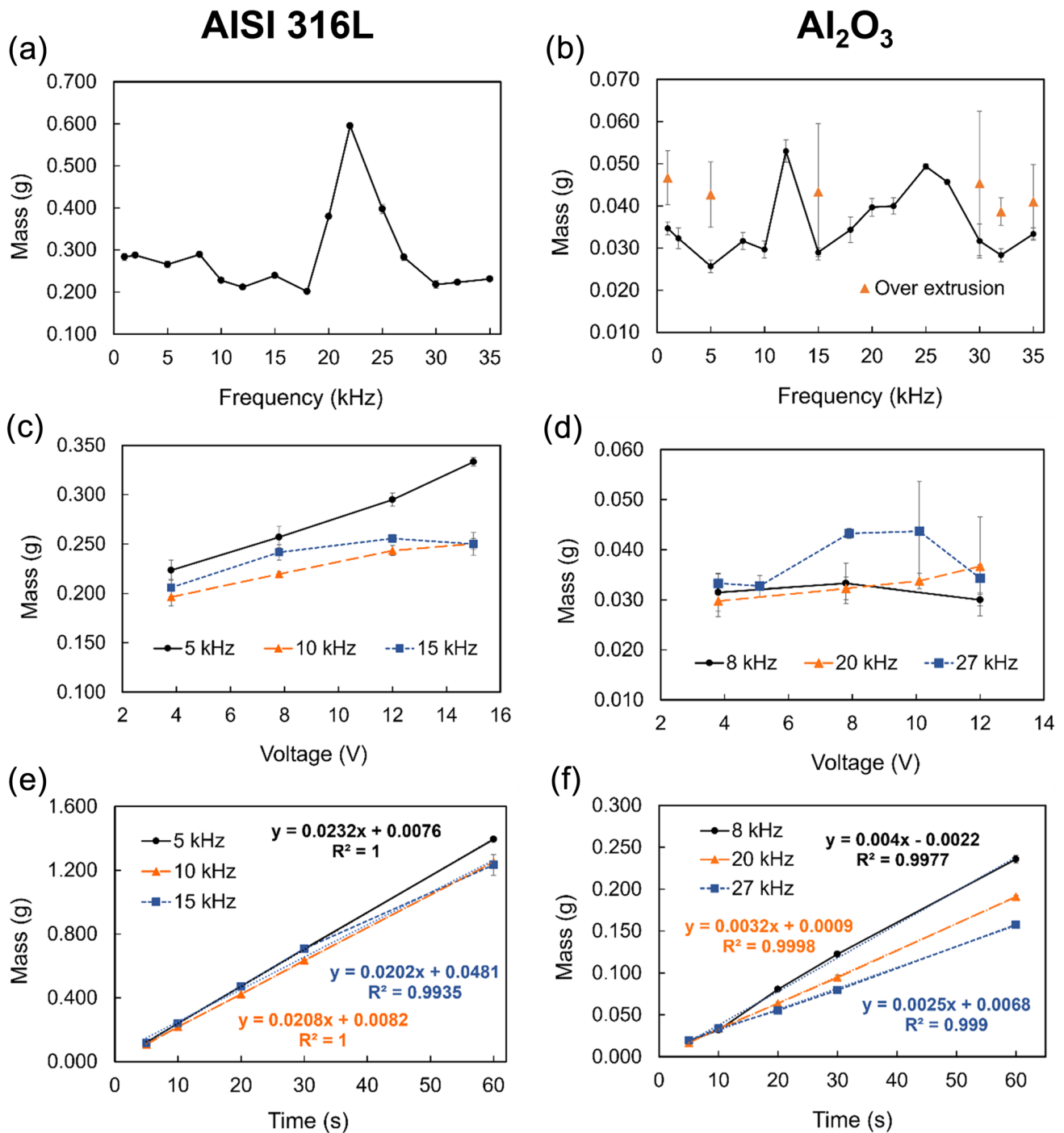


Fig. 6 Extrusion test for both AISI 316L and alumina powders. **a, b** Frequency sweep at a constant voltage of 7.8 V **c, d** amplitude sweep at three constant frequencies and **e, f** time sweep at constant voltage

of 7.8 V and frequencies reported in the figure to assess the linearity of the deposition process. For **a–d** the extrusion time was set at 10 s

powder flow does not stop immediately following the piezo-deactivation (Online Resource 7), resulting in an unpredictable over-extrusion of material. The occurrence of this

phenomenon is indicated by the isolated orange triangles in Fig. 6b.

The vibration amplitude, defined by the maximum voltage applied to the piezoelectric actuator, seems to play a minor role in controlling the mass of the material extruded and overall, in the deposition process (Fig. 6c, d). It is worth noticing that for alumina, increasing the voltage can lead to an over-extrusion phenomenon, as indicated by the points in Fig. 6d where the standard deviation increase.

To characterize the stability of the deposition process in the chosen conditions (5 kHz for AISI 316L and 20 kHz for alumina) we controlled the linearity in the amount of deposited powders over 60 s, estimated as the longest possible time of uninterrupted powder deposition during any typical printing process (Fig. 6e, f). Both AISI 316L and alumina show good linear behavior over this time.

This result suggests that the nozzle vibration does not produce progressive powder compaction during the deposition process.

3.3 Characterization of the final products

The overall process developed in this study is summarized in Fig. 7. It involves two steps: the deposition of the two powders forming the object of interest within a graphite die and the subsequent sintering of the deposited powder using the FAST/SPS method. Figure 7a shows the setup used for printing, with the two dispensers containing the powders used in the process. Figure 7b shows the structure produced by the printing process at an intermediate stage. The image shows the two powders deposited on each layer: the darker squared region is composed of the AISI 316L powder, which is surrounded by white alumina powder. Both powders are contained within the graphite die. The sintering process in the FAST/SPS machine is shown in Fig. 7c. Here the

graphite die is partially wrapped by graphite felt to reduce the radiation heat losses during the process. The square aperture in the radiation shield allows the insertion of a K-type thermocouple in the lateral wall of the die. The final product, after the removal of the alumina powder surrounding it, is shown in Fig. 7d.

Some examples of simple geometries realized using the DPD-FAST approach are shown in Fig. 8.

The geometry shown in (Fig. 8b) allows evaluating the deformations that the geometry undergoes during the sintering process. The original CAD model was, in this case, a symmetric cube. However, at the end of the process, a contraction of about 40 to 45% is observed in the direction parallel to the applied uniaxial load. No significant change in the other two directions was observed. This result suggests that the alumina powders surrounding the metallic geometry did not behave as an ideal fluid and did not produce a uniform distribution of the applied load. As a result, the process can be considered as “quasi-isostatic”. On the other hand, the extent of this deformation is quite reproducible, and it can be easily compensated by modifying the starting geometry accordingly.

One interesting characteristic of the DPD-FAST approach is represented by its ability to produce geometries presenting unsupported hanging elements. In fact, the alumina powder deposited all around the primary geometry behave as support for elements emerging from the bulk of the object. An example is represented by the handlebar-shaped object shown in Fig. 8d. This geometry was originally printed with the two end disks oriented perpendicularly to the direction of the applied load and parallel to the surface of the die punches. Despite that, no bending or warping of the two face disks can be observed.

STEP 1: Direct powder deposition (DPD) STEP 2: Sintering to get final components

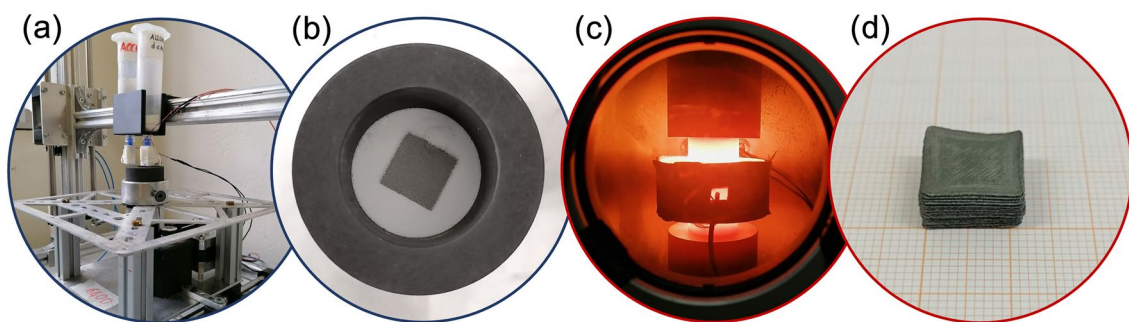


Fig. 7 Schematic of the entire process. **a** Printing stage, **b** powder distribution inside the graphite die after deposition, **c** graphite die during the SPS/FAST sintering, and **d** final sintered component

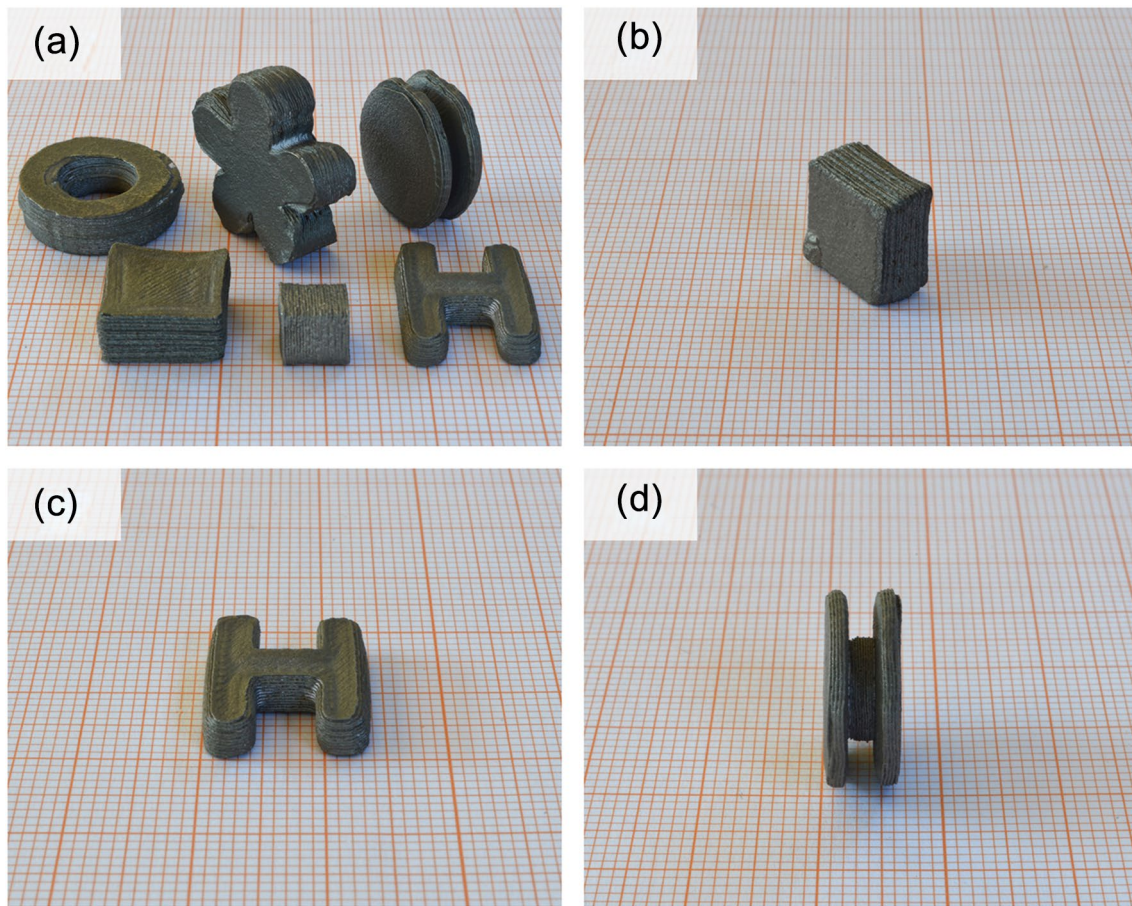


Fig. 8 (a) Collection of some of the samples produced using the DPD-FAST approach. (b) Simple square geometry, (c) H-like geometry and (d) handlebar-like geometry

The final relative density for all samples we produced using the DPD-FAST approach was around $96 \pm 2\%$, measured with the Archimedes method. The microstructure of the sintered samples is shown in the cross-section images reported in Fig. 9. Despite the very short sintering time (5 min), only a residual microporosity can be observed. The grains of the original powder are only slightly visible. It must be noted that the microstructure, and the corresponding relative density, is influenced by the layer height used during the printing process. Figure 9a, b shows the microstructure of a sample printed with a layer height of 0.28 mm, while in the case of the sample shown in Fig. 9c, d the layer height was set to 0.40 mm. In this last case, the micro-porosity around each original metallic grain is more evident, and the relative density is reduced to 90%. The use of different layer heights influences the packing of the particles during the deposition process hence the green density of the printed object.

4 Conclusion

The proposed direct powder deposition (DPD) method, combined with the FAST/SPS sintering approach, proved to be a fast and viable route for the realization of complex geometries, avoiding the use of any chemical in combination with the powders of the required material. As a result, no debinding process is required, while the FAST/SPS sintering allows to completion of the densification of the printed powders in less than 1 h. The implementation of additional printheads opens the possibility of creating a multi-material object. As shown in deposition tests, the process is robust and reliable. The ability to maintain the shape of the primary powder is guaranteed thanks to the containment provided by the support powder. Great care must be taken when choosing the appropriate powders for this type of application. The study of rheological and

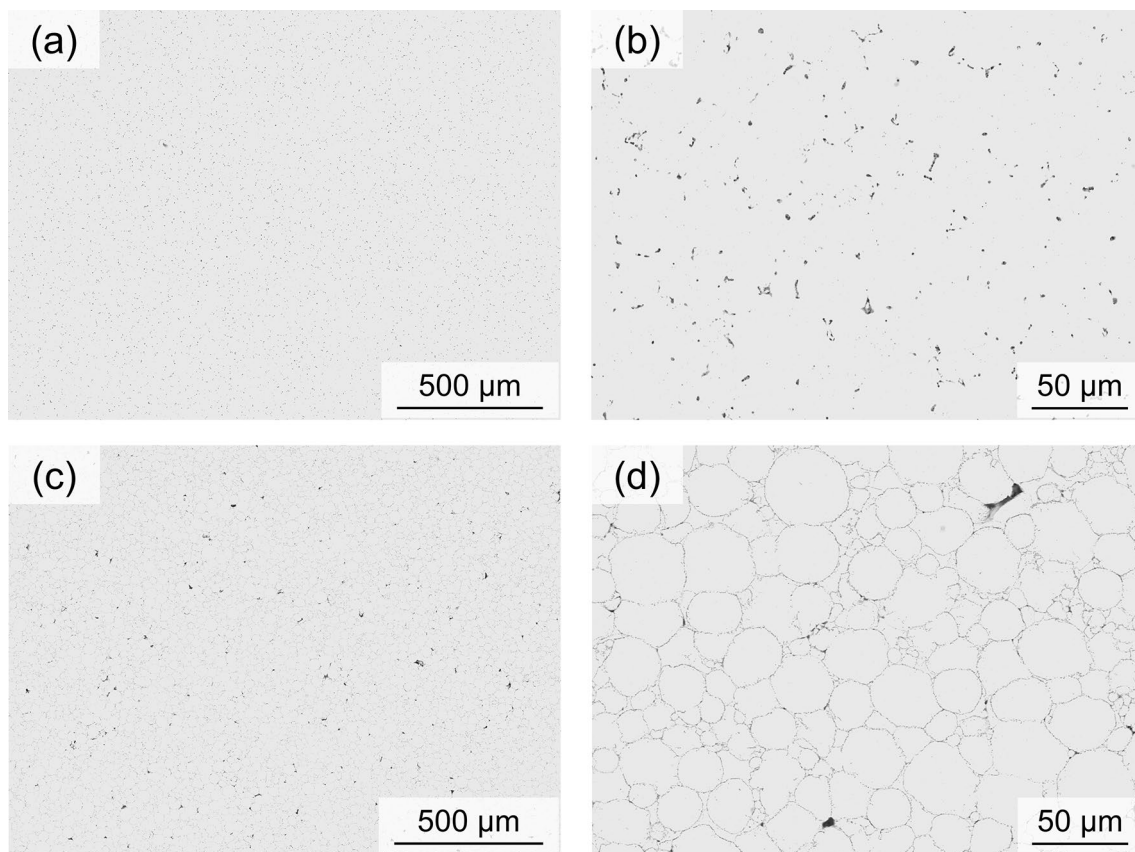


Fig. 9 SEM images of a cross-section of AISI 316L sintered object. **a, b** Sample printed with a layer height of 0.28 mm, presenting a final density of 96%. **c, d** Sample printed with a layer height of 0.40 mm, presenting a final density of 90%

morphologic properties is essential to avoid clogging or irregularity in the powder dispensing process.

Supplementary Information The online version contains supplementary material available at <https://doi.org/10.1007/s40964-023-00552-2>.

Acknowledgements This work was partially supported by the Italian Minister of University and Research through the project “A BRIDGE TO THE FUTURE: Computational methods, innovative applications, experimental validations of new materials and technologies” (No. 2017L7X3CS) within the PRIN 2017 program. Regione Lombardia also partially supported this work through the project “MADE4LO—Metal ADditivE for Lombardy” (No. 240963) within the POR FESR 2014-2020 program. The authors would also like to thank the CISRiC for using the SEM facility.

Funding Open access funding provided by Università degli Studi di Pavia within the CRUI-CARE Agreement. This article is funded by Ministero dell’Istruzione, dell’Università e della Ricerca, 2017L7X3CS, Regione Lombardia, 240963.

Data availability Data required to reproduce these findings have been given in the text. Any additional data can be shared upon request.

Declarations

Conflict of interest The authors declare that they have no known competing financial interests or personal relationships that could have appeared to influence the work reported in this paper.

Open Access This article is licensed under a Creative Commons Attribution 4.0 International License, which permits use, sharing, adaptation, distribution and reproduction in any medium or format, as long as you give appropriate credit to the original author(s) and the source, provide a link to the Creative Commons licence, and indicate if changes were made. The images or other third party material in this article are included in the article’s Creative Commons licence, unless indicated otherwise in a credit line to the material. If material is not included in the article’s Creative Commons licence and your intended use is not permitted by statutory regulation or exceeds the permitted use, you will need to obtain permission directly from the copyright holder. To view a copy of this licence, visit <http://creativecommons.org/licenses/by/4.0/>.

References

1. Dadbakhsh S, Mertens R, Hao L, Van Humbeeck J, Kruth J (2019) Selective laser melting to manufacture “in situ” metal matrix composites: a review. *Adv Eng Mater* 21:1801244. <https://doi.org/10.1002/adem.201801244>
2. Prashanth KG (2020) Selective laser melting: materials and applications. *J Manuf Mater Process* 4:13. <https://doi.org/10.3390/jmmp4010013>
3. Martin AA, Calta NP, Khairallah SA, Wang J, Depond PJ, Fong AY, Thampy V, Guss GM, Kiss AM, Stone KH, Tassone CJ, Nelson Weker J, Toney MF, Van Buuren T, Matthews MJ (2019)

- Dynamics of pore formation during laser powder bed fusion additive manufacturing. *Nat Commun* 10:1987. <https://doi.org/10.1038/s41467-019-10009-2>
4. Huo C, Tian X, Nan Y, Li D (2020) Hierarchically porous alumina ceramic catalyst carrier prepared by powder bed fusion. *J Eur Ceram Soc* 40:4253–4264. <https://doi.org/10.1016/j.jeurceramsoc.2020.03.059>
 5. Gong H, Rafi K, Gu H, Starr T, Stucker B (2014) Analysis of defect generation in Ti–6Al–4V parts made using powder bed fusion additive manufacturing processes. *Addit Manuf* 1–4:87–98. <https://doi.org/10.1016/j.addma.2014.08.002>
 6. Huo C, Tian X, Nan Y, Qiu Z, Zhong Q, Huang X, Yu S, Li D (2021) Regulation mechanism of the specific surface area of alumina ceramic carriers with hierarchical porosity fabricated by powder bed fusion. *Ceram Int* 47:30954–30962. <https://doi.org/10.1016/j.ceramint.2021.08.198>
 7. Mostafaei A, Zhao C, He Y, Reza Ghiaasiaan S, Shi B, Shao S, Shamsaei N, Wu Z, Kourayem N, Sun T, Pauza J, Gordon JV, Webler B, Parab ND, Asherloo M, Guo Q, Chen L, Rollett AD (2022) Defects and anomalies in powder bed fusion metal additive manufacturing. *Curr Opin Solid State Mater Sci* 26:100974. <https://doi.org/10.1016/j.cossms.2021.100974>
 8. Zhang X, Yocom CJ, Mao B, Liao Y (2019) Microstructure evolution during selective laser melting of metallic materials: a review. *J Laser Appl* 31:031201. <https://doi.org/10.2351/1.5085206>
 9. Yasa E, Kruth J-P (2011) Microstructural investigation of selective laser melting 316L stainless steel parts exposed to laser re-melting. *Procedia Eng* 19:389–395. <https://doi.org/10.1016/j.proeng.2011.11.130>
 10. Song B, Zhao X, Li S, Han C, Wei Q, Wen S, Liu J, Shi Y (2015) Differences in microstructure and properties between selective laser melting and traditional manufacturing for fabrication of metal parts: a review. *Front Mech Eng* 10:111–125. <https://doi.org/10.1007/s11465-015-0341-2>
 11. Wu H, Pritchett D, Wolff S, Cao J, Ehmann K, Zou P (2020) A vibration-assisted powder delivery system for additive manufacturing - an experimental investigation -. *Addit Manuf* 34:101170. <https://doi.org/10.1016/j.addma.2020.101170>
 12. Zhang X, Chueh Y, Wei C, Sun Z, Yan J, Li L (2020) Additive manufacturing of three-dimensional metal-glass functionally gradient material components by laser powder bed fusion with in situ powder mixing. *Addit Manuf* 33:101113. <https://doi.org/10.1016/j.addma.2020.101113>
 13. Airolidi L, Bruculeri R, Baldini P, Pini F, Vigani B, Rossi S, Auricchio F, Anselmi-Tamburini U, Morganti S (2021) 3D printing of copper using water-based colloids and reductive sintering, 3D print. *Addit Manuf*. <https://doi.org/10.1089/3dp.2021.0248>
 14. Salman OO, Gammer C, Chaubey AK, Eckert J, Scudino S (2019) Effect of heat treatment on microstructure and mechanical properties of 316L steel synthesized by selective laser melting. *Mater Sci Eng A* 748:205–212. <https://doi.org/10.1016/j.msea.2019.01.110>
 15. Zakeri S, Vippola M, Levänen E (2020) A comprehensive review of the photopolymerization of ceramic resins used in stereolithography. *Addit Manuf* 35:101177. <https://doi.org/10.1016/j.addma.2020.101177>
 16. Munir ZA, Anselmi-Tamburini U, Ohyanagi M (2006) The effect of electric field and pressure on the synthesis and consolidation of materials: a review of the spark plasma sintering method. *J Mater Sci* 41:763–777. <https://doi.org/10.1007/s10853-006-6555-2>
 17. Munir ZA, Ohyanagi M (2021) Perspectives on the spark plasma sintering process. *J Mater Sci* 56:1–15. <https://doi.org/10.1007/s10853-020-05186-1>
 18. ASTM B527–22 - Tap density of metal powders and compound, (n.d.). Book of Standards Volume: 02.05, Developed by Subcommittee: B09.03, Pages: 4, ICS Code: 77.160, Last update: Feb 16, 2023. <https://doi.org/10.1520/B0527-23>
 19. ASTM B213–20 - Flow rate of metal powders using the hall funnel, (n.d.). Book of Standards Volume: 02.05, Developed by Subcommittee: B09.02, Pages: 4, ICS Code: 77.160, Last update: Apr 07, 2020. <https://doi.org/10.1520/B0213-20>
 20. ASTM B212–21—apparent density of free flowing metal powders using the carney funnel, (n.d.). Book of Standards Volume: 02.05, Developed by Subcommittee: B09.02, Pages: 4, ICS Code: 77.160, Last update: Sep 15, 2021. <https://doi.org/10.1520/B0212-21>
 21. Bruculeri R, Airolidi L, Baldini P, Vigani B, Rossi S, Morganti S, Auricchio F, Anselmi-Tamburini U (2023) Spark plasma sintering of complex metal and ceramic structures produced by material extrusion, 3D print. *Addit Manuf*. <https://doi.org/10.1089/3dp.2022.0279>
 22. Lefebvre LP, Whiting J, Nijkovsky B, Brika SE, Fayazfar H, Lyckfeldt O (2020) Assessing the robustness of powder rheology and permeability measurements. *Addit Manuf* 35:101203. <https://doi.org/10.1016/j.addma.2020.101203>
 23. Zegzalka J, Gelnar D, Jezerska L, Prokes R, Rozbroj J (2020) Characterization and flowability methods for metal powders. *Sci Rep* 10:21004. <https://doi.org/10.1038/s41598-020-77974-3>
 24. Du H, Lu H, Tang J, Liu H (2023) Characterization of powder flow properties from micron to nanoscale using FT4 powder rheometer and PT-X powder tester. *Particuology* 75:1–10. <https://doi.org/10.1016/j.partic.2022.05.014>
 25. Bernard-Granger G, Giraud M, Pascal E, Mailhan L, Larsson T, Valot C, Ablitzer C, Gatamel C, Berthiaux H (2019) Rheological properties of alumina powder mixtures investigated using shear tests. *Powder Technol* 345:300–310. <https://doi.org/10.1016/j.powtec.2019.01.027>
 26. Abdullah EC, Geldart D (1999) The use of bulk density measurements as flowability indicators. *Powder Technol* 102:151–165. [https://doi.org/10.1016/S0032-5910\(98\)00208-3](https://doi.org/10.1016/S0032-5910(98)00208-3)
 27. Iams AD, Gao MZ, Shetty A, Palmer TA (2022) Influence of particle size on powder rheology and effects on mass flow during directed energy deposition additive manufacturing. *Powder Technol* 396:316–326. <https://doi.org/10.1016/j.powtec.2021.10.059>
 28. Groarke R, Danilenkoff C, Karam S, McCarthy E, Michel B, Musatto A, Sloane J, O'Neill A, Raghavendra R, Brabazon D (2020) 316L stainless steel powders for additive manufacturing: relationships of powder rheology, Size, size distribution to part properties. *Materials* 13:5537. <https://doi.org/10.3390/ma13235537>
 29. Boehmler J, Moitrier F, Bourré T, Rossit J, Delorme F, Lemonnier S (2021) Influence of powder state and rheology on sintering behaviour of SiC. *Open Ceram* 8:100192. <https://doi.org/10.1016/j.oceram.2021.100192>
 30. De Campos MM, Ferreira MDC (2013) A comparative analysis of the flow properties between two alumina-based dry powders. *Adv Mater Sci Eng* 2013:1–7. <https://doi.org/10.1155/2013/519846>
 31. Ramavath P, Swathi M, Buchi Suresh M, Johnson R (2013) Flow properties of spray dried alumina granules using powder flow analysis technique. *Adv Powder Technol* 24:667–673. <https://doi.org/10.1016/j.appt.2012.12.006>
 32. Schulze D (1990) Standard shear testing technique for particulate solids using the Jenike shear cell: edited by The Institution of Chemical Engineers, Rugby, UK, 1989; 46 pp. paperback; £ 16.50 plus postage; ISBN 0 85295 232 5, Elsevier
 33. Caitano R, Guerrero BV, González RER, Zuriguel I, Garcimartín A (2021) Characterization of the clogging transition in vibrated granular media. *Phys Rev Lett* 127:148002. <https://doi.org/10.1103/PhysRevLett.127.148002>
 34. Yang J, Gong D, Wang X, Wang Z, Li J, Hu B, Xia C (2022) Three-dimensional clogging structures of granular spheres near hopper

- orifice. *Chin Phys B* 31:014501. <https://doi.org/10.1088/1674-1056/ac2f2f>
35. Janda A, Maza D, Garcimartín A, Kolb E, Lanuza J, Clément E (2009) Unjamming a granular hopper by vibration. *EPL Europhys Lett* 87:24002. <https://doi.org/10.1209/0295-5075/87/24002>
 36. Fayed ME, Otten L (1997) *Handbook of powder science technology*. CarmanHall, NY
 37. Matchett AJ (2004) A theoretical model of vibrationally induced flow in conical hopper systems. *Chem Eng Res Des* 82:85–98. <https://doi.org/10.1205/026387604772803098>
 38. Lu X, Yang S, Evans JRG (2006) Studies on ultrasonic microfeeding of fine powders. *J Phys Appl Phys* 39:2444–2453. <https://doi.org/10.1088/0022-3727/39/11/020>
 39. Lu X, Yang S, Evans JRG (2009) Microfeeding with different ultrasonic nozzle designs. *Ultrasonics* 49:514–521. <https://doi.org/10.1016/j.ultras.2009.01.003>

Publisher's Note Springer Nature remains neutral with regard to jurisdictional claims in published maps and institutional affiliations.